

<https://doi.org/10.1038/s43246-025-01018-4>

Molecular dynamics study of graphite 2-D nucleation from paramagnetic Fe-C melt

Adam Götz^{1,2}✉, Daniel Marchand³, Leander Michels^{4,5} & Jaakko Akola^{1,6}

The nucleation and growth of graphite in Fe-C alloys (cast iron) can both be related to the 2-D nucleation of a single atomic layer of graphene. Here, we use molecular dynamics (MD) simulations to study the nucleation of graphite from molten iron. A neural-network potential is developed for the Fe-C system using a pragmatic approach to treat the paramagnetic nature of liquid iron, and its thermodynamic behavior is validated against data from thermochemical software. The critical nucleus size and free-energy barrier for nucleation are computed using MD simulations in combination with enhanced sampling methods, and the results are compared with continuum models based on adaptations of classical nucleation theory. 2-D nucleation is found to be a feasible mechanism for graphite nucleation and growth at a carbon supersaturation of 5 at. % or higher. At low supersaturation the nucleation rate declines, and other mechanisms such as interaction with substrates other than graphite, solute elements, or defects are necessary to facilitate the formation of new layers.

Crystallization plays a fundamental role in determining the physical properties of materials. In metallic systems, it governs phase formation and microstructure evolution, thereby controlling key properties such as mechanical strength and thermal conductivity¹. In Fe-C alloys (cast iron), the nucleation and growth of graphite determine both the competition between graphite and cementite formation and the resulting graphite morphology, each of which have profound implications for the properties of the as-cast material^{2,3}. Despite significant progress in understanding these phenomena⁴⁻⁶, the crystallization of Fe-C alloys remains poorly understood due to the high temperatures and complexity of phase transitions involved, and there is a need for fundamental understanding of the nucleation and growth of phases at the atomistic level⁷⁻⁹.

Although Fe-C alloys are an interesting system for studying nucleation mechanisms due to their multiscale complexity, the scientific challenge of understanding nucleation from high-temperature metallic melts is much broader. Across several alloy families, heterogeneous substrates, undercooling conditions, and solute effects lead to markedly different nucleation pathways. For example, in aluminum alloys, the inoculation with Al-5Ti-1B master alloys has become the industrial paradigm: TiB₂ particles, often stabilized by thin Al₃Ti layers, serve as potent heterogeneous nucleation sites for α -Al grains, with their efficiency governed not only by lattice matching but also by growth-restriction factors and the onset of free growth¹⁰. In-situ synchrotron X-radiography and diffraction experiments have further revealed how recalescence, solute segregation, and particle size distributions

influence the spread of nucleation undercoolings and ultimately determine grain size¹¹⁻¹³. In steels, rare-earth oxides and oxy-sulfides, such as Ce₂O₃ and Ce₂O₂S, have been demonstrated to refine austenite grains by acting as heterogeneous nuclei, improving both toughness and strength¹⁴.

Beyond specific alloy systems, a broader theoretical framework has emerged, distinguishing nucleation from grain initiation. Early-stage solidification encompasses prenucleation ordering, the formation of two-dimensional nuclei, and subsequent three-dimensional cap growth¹⁵. Undercooled metallic melts, such as Ni and Cu-Ni, exhibit a universal grain refinement transition associated with dendrite fragmentation during recalescence, demonstrating that nucleation phenomena can be deterministic and system-independent¹⁶. Recent studies also highlight new frontiers: nanoparticle additions (Ti-C-N based) provide powerful growth restriction and even act as nucleants, potentially overcoming the limitations of conventional inoculation strategies¹⁰. These diverse insights demonstrate that nucleation remains an open scientific question across metallic systems and liquid states, spanning from normal to deeply undercooled regimes, making it a rich area of research that extends well beyond the traditional Fe-C alloy framework¹⁷.

Graphite nucleation in the production of Fe-C alloys is facilitated by the addition of inoculants that form non-metallic inclusions acting as heterogeneous nucleation sites for graphite^{4,18,19}. The suitability of an inclusion for graphite nucleation is usually justified in terms of interfacial energies²⁰, or more traditionally crystallographic match^{21,22}, although most theories lack a

¹Department of Physics, Norwegian University of Science and Technology (NTNU), Trondheim, Norway. ²Innovation Department, Elkem Silicon Products (ESP), Kristiansand, Norway. ³SINTEF Industry, Oslo, Norway. ⁴Chemical Sciences Division, Lawrence Berkeley National Laboratory, Berkeley, CA, USA. ⁵Institute of Physics, University of Brasilia (UnB), Brasilia, DF, Brazil. ⁶Computational Physics Laboratory, Tampere University, Tampere, Finland.

✉ e-mail: adam.gotz@ntnu.no

description of the atomistic mechanism for nucleation²³. The morphology of graphite can also be modified by the introduction of deoxidizing elements, usually magnesium, causing a transformation from lamellar to spheroidal graphite iron^{24,25}. This change in graphite morphology is associated with a shift in the apparent growth direction from the prismatic *a*-direction to the basal *c*-direction which departs from the Bravais rule stating that lower-density crystallographic planes have higher growth rates, and thus again raises uncertainty of the underlying mechanism.

For atomically smooth (faceted) crystals, such as the basal plane of graphite, the interface advances through lateral growth²⁶. Two mechanisms for lateral growth are recognized: 2-D nucleation where islands form and expand laterally across the surface, and defect-controlled growth where crystal defects act as step sources for the formation of new layers. An illustration of graphite 2-D nucleation is shown in Fig. 1. Models for graphite growth along the *c*-direction based on 2-D nucleation have been proposed to explain radial growth in spheroidal and thickening of lamellae in lamellar graphite irons^{27–29}. More recently, similar disc-shaped nucleation models have also been applied to quantify the heterogeneous graphite nucleation potency of oxide and sulfide inclusions²⁰. Several defect-controlled mechanisms relevant for graphite growth in spheroidal graphite iron have also been proposed in the past, including the cone-helix growth model by Double and Hellawell³⁰, modified screw dislocation spiral growth³¹, helical macro-spiral growth³² and curved-circumferential growth models³³. However, the large variety of observations available that support distinct mechanisms^{34,35} and the absence of sufficiently accurate material data for analytical validation lead to uncertainty in the application of such models.

Molecular dynamics (MD) simulations provide a convenient platform for studying the atomic-scale mechanism for graphite nucleation and growth³⁶ as they enable direct investigation of nucleation kinetics and free-energy barriers in ways that are difficult to capture experimentally. For example, Tewary et al.³⁷ used MD with classical force fields to study the impact of solute elements on solid/liquid interfacial energies in the melt, and used the difference between the basal and prismatic planes of graphite to justify the resulting change in graphite morphology. Historically, such studies have been constrained by the difficulty of developing force fields that accurately capture the physics of the system³⁸. Systems containing liquid iron are particularly challenging even through first-principles methods (spatially and temporally limited) due to the paramagnetic nature of iron at high temperatures^{39,40}. Although for the Fe-C system the available Embedded Atom Method (EAM) potentials and their modified (MEAM) variants give good descriptions of the iron-rich phases⁴¹, they are developed for metals and thus unsuitable for representing the covalent bonds of graphite which is the main focus of this study. Recent advances in machine-learning (ML) force fields⁴² and the emergence of universal potentials⁴³ have significantly reduced this limitation, facilitating the creation of more accurate force fields with considerably less effort.

In the present work, a neural-network potential (NNP) tailored to the Fe-C system is developed using a pragmatic approach to treat the paramagnetic nature of molten iron. The approach involves first training spin-aware NNP based on spin-polarized Density Functional Theory (DFT) data, and then averaging over magnetic configurations to create a training set for a second paramagnetic NNP. Thermodynamic data relevant for

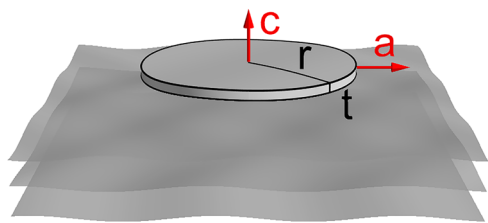


Fig. 1 | Model for graphite 2-D nucleation. The process involves the formation of a disc-shaped new layer of graphene with radius *r* and thickness *t* that spreads along the *a*-direction, thus effectively constituting growth along the *c*-direction.

crystallization is computed using MD simulations in combination with enhanced sampling methods, and the results are validated against experimentally-derived data obtained from thermochemical software. Graphite 2-D nucleation is then explored in the context of MD simulations to bridge the gap between continuum models and atomistic mechanisms. The objective of this investigation is to enhance the understanding of graphite growth along the *c*-direction as well as to serve as a benchmark case for elucidating the mechanism for heterogeneous nucleation of graphite on other substrates pre-existing in the melt.

Results

The role of magnetic ordering

Before proceeding to validate the developed paramagnetic NNP, it is of interest to assess the importance of fluctuating magnetic moments in the modeled system. To this end, Density Functional Theory (DFT) calculations using various magnetic configurations were performed on a single molecular dynamics snapshot of a graphite (0001) / melt interface consisting of 44 atoms. The average of 101 random paramagnetic configurations, where the spin moments of iron atoms were randomly assigned as spin up or spin down, was considered as the true paramagnetic state, and the difference in forces on individual iron atoms of the various magnetic configurations were compared to the paramagnetic average. It was found that a single paramagnetic configuration had an average error of 24.1%. In contrast, using a single diamagnetic or ferromagnetic configuration yielded an error of 55.9 or 59.3%, respectively. This demonstrates the need for averaging over several magnetic configurations when dealing with paramagnetic liquids. The NNP developed in this work yielded a lower error of 7.5%.

To further demonstrate this point, the equilibrium lattice parameter of austenite supercells with distinct magnetic ordering was calculated. The total energy as a function of lattice parameter *a* is shown in Fig. 2. The diamagnetic, ferromagnetic and antiferromagnetic energies are obtained from single DFT calculations and have minima at 3.43, 3.59 and 3.50 Å, respectively. The paramagnetic configuration is the average of 10 DFT runs with Fe spins randomized as spin up or down yielding an equilibrium lattice parameter of 3.50 Å equally to the antiferromagnetic curve. The NNP prediction is added as a reference yielding a lattice parameter of 3.52 Å, in close agreement with the antiferromagnetic and paramagnetic curves. It should be noted that while in solids an antiferromagnetic configuration may constitute a satisfactory approximation to the paramagnetic state, in a disordered structure such as a liquid an antiferromagnetic configuration cannot be uniquely defined and any choice of a single configuration will give rise to random variation in the training set, thus necessitating to average over multiple configurations.

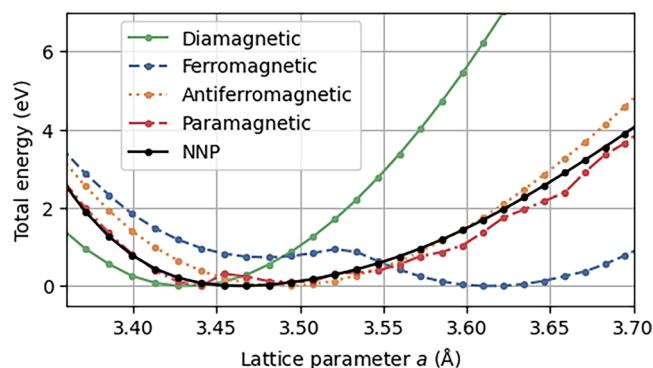


Fig. 2 | Influence of magnetic ordering on lattice parameter. The total DFT energy as a function of lattice parameter of a γ -Fe (austenite) supercell consisting of 32 atoms is shown at distinct magnetic configurations. The paramagnetic state is obtained as the average of 10 DFT runs with Fe spins randomly assigned as up or down. Distinct equilibrium lattice parameters for γ -Fe are obtained depending on the magnetic ordering.

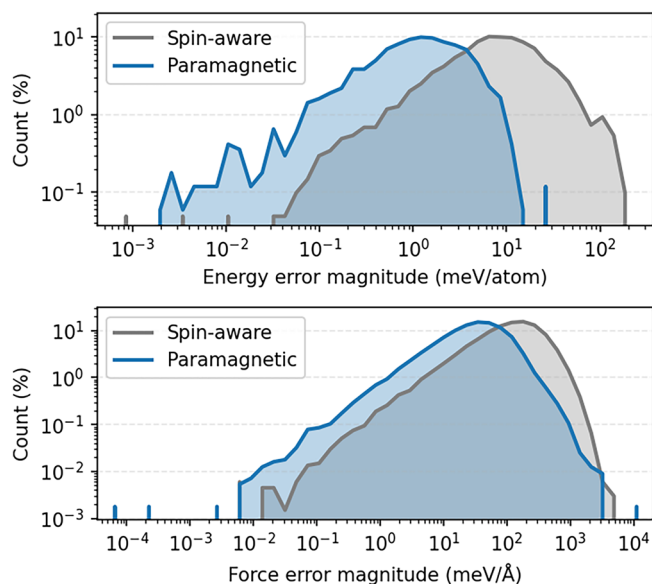


Fig. 3 | Distribution of errors for the spin-aware and paramagnetic NNPs. The spin-aware model obtained a RMSE of 23 meV atom^{-1} in energies and 259 meV Å^{-1} in forces, while the paramagnetic model had a RMSE of 3 meV atom^{-1} in energies and 103 meV Å^{-1} in forces.

Neural-network potential validation

In this section, the quality of the developed paramagnetic NNP is validated. The validation errors of the spin-aware and paramagnetic NNPs are shown in Fig. 3. The root-mean-square-error (RMSE) energies are 23 meV atom^{-1} in the spin-aware model (trained on DFT data) and 3 meV atom^{-1} in the paramagnetic model (trained on spin-averaged results of the former model). The RMSE forces are $259 \text{ meV atom}^{-1}$ and 103 meV Å^{-1} , respectively. These errors are in line with those expected for a potential targeting liquid iron structures. For example, Byggmästar et al. found that even very expensive GAP-SOAP potentials exhibit errors of 4 meV atom^{-1} and 200 meV Å^{-1} for energies and forces over liquid structures⁴⁴.

The performance of the NNPs in predicting lattice and elastic constants of graphite and γ -Fe is summarized in Table 1. For graphite, the spin-aware and paramagnetic models give similar results. They both tend to under-predict, relative to DFT and experiment, the *c*-lattice constant and have some substantial errors in the elastic constants. For γ -Fe, in general good alignment of the lattice constants with greater errors on elastic constants is observed. Importantly, it is noted that the paramagnetic model gives nearly identical results to the spin-aware model averaged over large cells of randomly-assigned spins, thus validating the present approach for treating paramagnetism. These results provide a sanity check that the NNPs can reasonably capture the physics of the Fe-C system at high temperatures. Since the purpose of this work is to study nucleation from the melt and not mechanical properties, it is not critical to reproduce elastic constants accurately.

To evaluate the ability of the NNP to reproduce the solid / liquid phase transitions of pure iron at high temperature, coexistence simulations of solid phases with the melt were run at different temperatures and the local order of the structure was monitored (see Supplementary Information for the collective variable used). The melting point was determined as the temperature at which the probability of the system of melting or solidifying is 50%. The melting points of Face-Centered Cubic (FCC) and Body-Centered Cubic (BCC) iron were determined as $1816 \pm 5 \text{ K}$ and $1880 \pm 20 \text{ K}$, respectively. The corresponding values obtained from FactSage are 1801 and 1811 K , demonstrating that the NNP reproduces melting points and the relative stability of FCC and BCC iron with reasonable accuracy. The prediction for BCC iron is likely to be negatively influenced by the lack of the structure in the DFT training set.

Table 1 | Structural properties of solid phases

Property	Method			
	Spin-aware ^a	Paramag.	DFT ^{b, c}	Exp. ^{d, e}
Graphite				
<i>a</i>	2.45	2.45	2.46	2.46
<i>c</i>	6.40	6.43	6.82	6.71
<i>C</i> ₁₁	1450	1426	1069	1060 ± 16
<i>C</i> ₁₂	294	316	162	180 ± 20
<i>C</i> ₁₃	0.0	0.0	-4	15 ± 5
<i>C</i> ₃₃	204	222	40	36.5 ± 1
<i>C</i> ₄₄	8.2	8.3	5	4.0 ± 0.4
γ -Fe				
<i>a</i>	3.50	3.50	3.48^{PM}	3.56
			3.48^{AF}	
<i>C</i> ₁₁	254	252	309^{AF}	154
<i>C</i> ₁₂	191	182	152^{AF}	122
<i>C</i> ₄₄	127	127	201^{AF}	77

Lattice constants (Å) and elastic constants (GPa) of graphite and γ -Fe are shown based on spin-aware and paramagnetic NNP versions, DFT, and experiments

^a γ -Fe results for the spin-aware model were taken by randomly assigning spins to a supercell of 864 atoms and then taking the average of five runs.

^b Graphite DFT computed in¹⁸ using the planewave method and the dispersion-corrected atom-centered pseudopotential¹⁹.

^c γ -Fe DFT paramagnetic (PM) lattice constant from⁴⁹, anti-ferromagnetic (AF) lattice and elastic constants from⁸⁰.

^d Experimental graphite lattice constants from⁸¹, experimental elastic constants from⁸².

^e Experimental γ -Fe lattice constants from⁸³, elastic constants from⁸⁴, results extrapolated to 0 K as stated in⁸⁰.

MD simulations were performed to gain a better understanding of the liquid structure. The structure factor ($S(q)$) and partial radial distribution functions (PDF) of the melt were calculated and are shown in Fig. 4. The structure factor of pure Fe was computed in a cell of 2076 atoms at 1873 K, as shown in Fig. 4a with available Ab Initio Molecular Dynamics (AIMD) and experimental work in the literature. We see that the computed structure factor with the NNP lies well within the available reference data. We also computed high-pressure results (3.7GPa) for pure Fe, Fe-14.4 at.%C and Fe-20 at.%C, and found that the location of the Q_1 peak using the NNP was 3.09, 3.06 and 3.09 Å^{-1} , while in the experimental work by Shibazaki et al.⁴⁵ the Q_1 peak locations were at 3.011, 2.984, and 2.979 Å^{-1} for the same concentrations and pressure. Importantly it shows that both the NNP and the experimental work indicate that the Q_1 peak is relatively insensitive to C concentration, shifting less than 0.03 Å^{-1} in both cases. This provides further confirmation of the quality of the potential, particularly when considering that it was not designed for high pressure simulations.

The PDF results were computed for an Fe-C melt containing 20 at.% carbon within the isothermal-isobaric (NPT) ensemble at 1500 K. The simulation box comprised 777 iron and 194 carbon atoms. The equilibrium density of the melt was $93.6 \text{ atoms nm}^{-3}$ which corresponds to a specific mass of 7.32 g cm^{-3} . In Fig. 4b we compare our results with those in the literature, specifically AIMD by Pan et al.⁴⁶ as well as an EAM potential created by Hepburn et al.⁴⁷ and run by Jiang et al.⁴¹ For all elements, the location and the magnitude of the $g(r)$ peak is much closer with the NNP than with the EAM. For Fe-C the EAM potential has numerous spurious peaks that are likely artifacts. The C-C PDF for AIMD has a small peak at $\approx 1.4 \text{ Å}$ that neither the NNP nor the EAM potential display. Overall the NNP shows strong agreement with the AIMD results, and significantly outperforms the EAM potential in reproducing the melt structure.

The diffusion constant for Fe and C was estimated by fitting a linear function to the mean square displacement as a function of time, and was found to be $D_{Fe} = 1.33 \times 10^{-5} \text{ cm}^2 \text{ s}^{-1}$ and $D_C = 2.71 \times 10^{-5} \text{ cm}^2 \text{ s}^{-1}$ for Fe

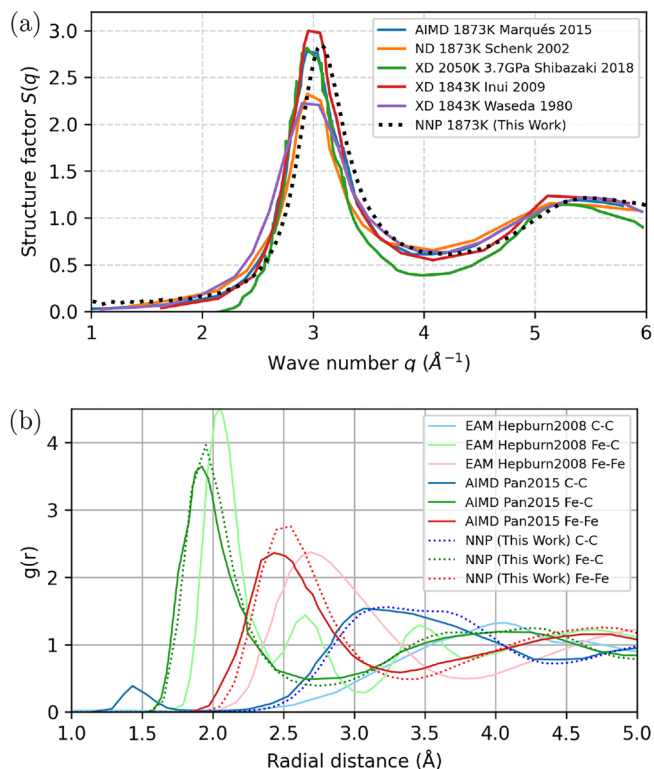


Fig. 4 | Structure of the molten phase. **a** Structure factor of pure Fe melt AIMD data taken from Marqués et al.⁸⁵, neutron diffraction (ND) data from Schenk et al.⁸⁶ and X-ray diffraction (XD) data from Inui et al.⁸⁷, Shibazaki et al.⁴⁵, and Waseda et al.⁸⁸. With the exception of the high pressure Shibazaki data, all results are at atmospheric pressure. **b** Partial radial distribution functions of Fe-20 at.%C from AIMD by Pan et al.⁴⁶, the EAM potential of Hepburn et al.⁴⁷ as computed by Jiang et al.⁴¹, and the NNP.

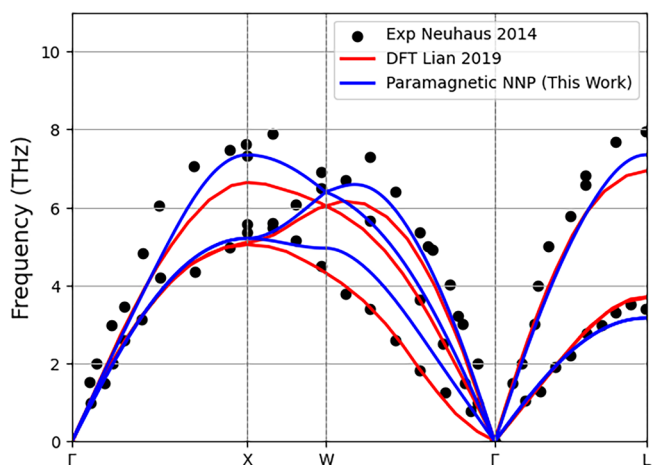


Fig. 5 | Phonon dispersion curve for γ -Fe. Data from experiment⁸⁹, DFT within an AFM approximation⁴⁹ and from the paramagnetic NNP. All results are based on the experimental lattice constant at 1573K (3.672 \AA).

and C, respectively. Neutron scattering has given an experimental value of $D_{\text{Fe}} = 1.34 \times 10^{-5} \text{ cm}^2 \text{ s}^{-1}$ for a 16.9% C melt⁴⁸ in good agreement with the simulated values. An EAM potential predicted a significantly higher diffusion constant for Fe than our work or experiments $D_{\text{Fe}} = 2.60 \times 10^{-5} \text{ cm}^2 \text{ s}^{-1}$ for a 4% C liquid at 1873 K, but agreed that C diffusion should be higher $D_{\text{C}} = 3.19 \times 10^{-5} \text{ cm}^2 \text{ s}^{-1}$ ⁴¹.

In order to further validate the spin-averaged potential, we examine the phonon dispersion curve of γ -Fe as shown in Fig. 5. We find that the curves show excellent agreement with experimental data, surpassing even previous

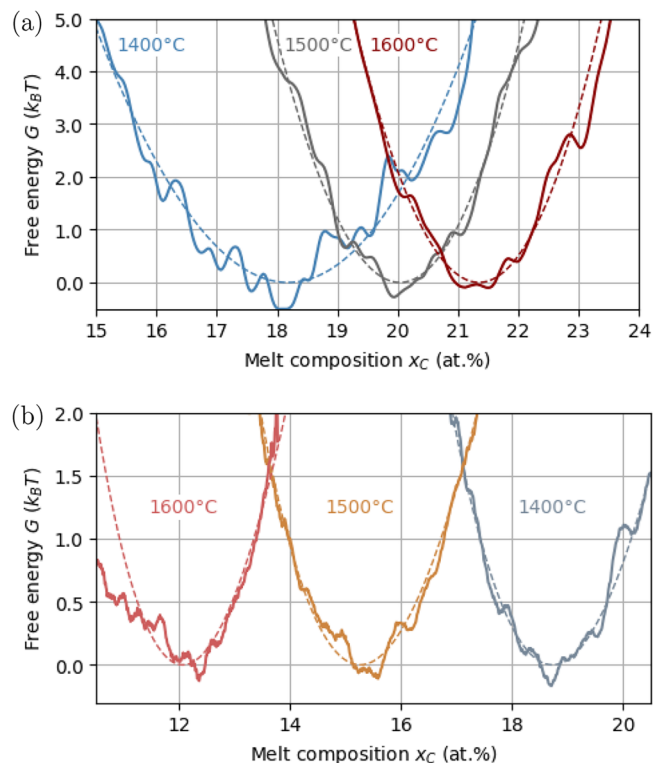


Fig. 6 | Free energy of crystallization. Free energies of the (a) graphite/melt and (b) austenite/melt slab systems (Fig. 12) are shown as a function of melt composition at constant total number of atoms. The melt composition is varied by moving C atoms between the melt and graphite phases. The MD simulation results are represented by solid lines and best-fit models by dashed lines. Minima of the curves correspond to the graphite and austenite liquidus compositions at the given temperatures.

DFT results in accuracy. Notably, our results align closely with prior DFT work using the spin-space averaging approach, and importantly this potential shows none of the imaginary phonon frequencies, indicative of lattice instability, that have been seen with ferromagnetic and non-magnetic models^{49,50}. The excellent agreement with experiment lends further confidence in downstream thermodynamics being correct for this phase in terms of vibrational contributions to the entropy.

Overall, the NNPs have RMSE for energies and forces in line with or below other state-of-the-art force fields focusing on liquids. They provide reasonable predictions of lattice constants, very good prediction of the iron phonon dispersion curve, though somewhat poor predictions of elastic constants, and excellent predictions of liquid radial distances and structure factor. They also demonstrate close agreement with experiment for Fe self-diffusion, while C self-diffusion does not have a clear prior value in experiment or simulations. Thus, the potential seems well-poised for studies of graphite nucleation from the Fe-C melt.

Fe-C phase equilibria

The free-energy profiles of the graphite/melt coexistence system are shown in Fig. 6a as a function of the melt composition at three different temperatures. Each curve is reconstructed from several simulations biased toward distinct values of the collective variable (the number of solid C atoms n_{c}) using umbrella sampling and the Weighted Histogram Analysis Method (WHAM). The number of solid atoms is converted into a composition using Eq. (12). Best-fit curves are shown as dashed lines. The minima of the curves correspond to the carbon content of the melt in equilibrium with graphite, and thus to points on the graphite liquidus line. The free-energy curve at 1400 K is wider and has more variation than the higher temperature curves due to less efficient sampling (limited time scale) of the umbrella windows at temperatures close to the eutectic temperature.

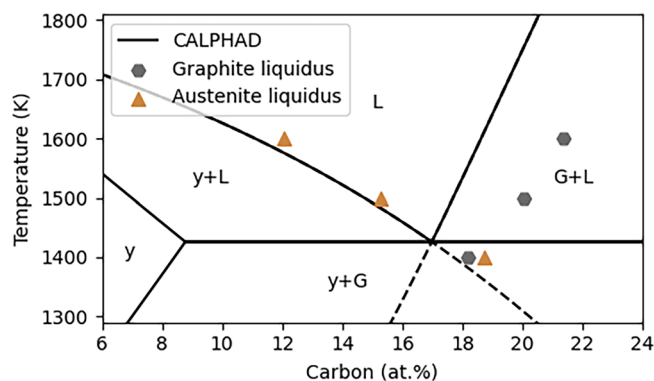


Fig. 7 | Phase diagram of the Fe-C eutectic system. The solid black lines correspond to the experimentally known phase diagram calculated using the thermochemical software FactSage⁷⁵. The gray and orange points correspond to the equilibrium points estimated from MD simulations.

Similar free-energy profiles are shown for the austenite / melt co-existence system in Fig. 6b. In this case, the collective variable used was the number of solid Fe atoms n_y . However, due to the significant solubility of carbon in austenite, the number of dissolved C atoms n_C^y must also be considered in the conversion of n_y to a composition. This was estimated in a post-processing step, and the melt composition was calculated analogously to Eq. (12) as $x_C = (n_C - n_C^y)/(n_{Fe} - n_y + n_C - n_C^y)$. The minima of the curves correspond to the carbon content of the melt in equilibrium with austenite, and thus to points on the austenite liquidus line. At 1600 K in the low x_C limit the curve deviates from the parabolic behavior, indicating that solid austenite is approaching the limit of its stability.

The equilibrium compositions are plotted in Fig. 7 as a function of temperature along with the experimentally known phase diagram calculated using FactSage. Good agreement is demonstrated between the simulation results and the phase diagram for the austenite liquidus line, while a systematic offset of about 2 at.% toward higher carbon contents is observed for the graphite liquidus line. This may be due to errors in the underlying DFT, for example assumptions in the exchange-correlation energy may cause subtle shifts in the free-energy curves of these phases.⁵¹ In recent work on the Cu-Al system switching from an ACE to a GAP potential reduced errors in the phase diagram, but at 10x the computational cost.⁵² This relatively modest error, relative to what is common in the literature for atomically-derived phase diagrams⁵³, places this potential at a good accuracy/cost ratio. Other potential sources contributing to this error include the NNP training methodology and MD sampling method.

In addition to identifying equilibrium compositions, it is of interest to estimate the driving force toward equilibrium at deviations from it. This driving force (difference in chemical potential) is defined as the proportionality constant $g_n = \Delta G_n / \Delta x_C$. In the context of MD simulations g_n is computed by fitting a parabola to the free-energy profile as a function of the number of solid atoms and using Eq. (2) described in Section “Thermodynamic modeling”. At 1500 K, the value $g_n = -2.69$ eV atom⁻¹ is obtained for the graphite / melt system. To extract this information from the experimentally derived free-energy data obtained from FactSage, Eq. (6) is used resulting in $g_n = -2.89$ eV atom⁻¹. The close agreement between the experimental and simulated values demonstrates the validity of the chosen approach.

Graphite 2-D nucleation

The free energy of graphite 2-D nucleation is shown in Fig. 8 as a function of the size of the nucleus for different supersaturations of carbon. Each curve represents the free energy required to form a 2-D nucleus of given size on a clean basal plane of graphite. The maxima of the curves represent the critical nucleus size and the associated free-energy barrier at a given supersaturation. At high supersaturation above ~10 at.% the critical nucleus size is small (3–10 atoms) and the nucleation barrier is negligible ($< 5k_B T$). At

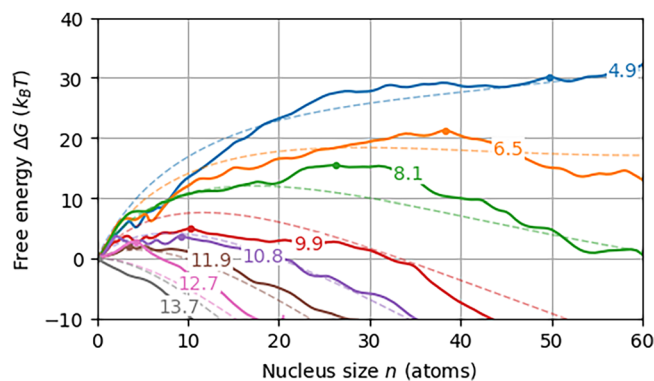


Fig. 8 | Free energy of graphite 2-D nucleation. Solid lines show the free energy as a function of nucleus size obtained from MD simulations with umbrella sampling and WHAM at various supersaturations of carbon in the melt. The maxima of the curves correspond to the critical nucleus size and free-energy barrier for nucleation. Dashed best-fit curves are calculated using Eq. (13) with parameters fitted to the data.

Table 2 | Graphite-melt interfacial energies

Method	T	$\gamma_{(10\bar{1}0)}$	$\gamma_{(11\bar{2}0)}$	$\gamma_{(0001)}$
MD	1400 K	168 ± 4	139 ± 3	172 ± 9
	1500 K	171 ± 3	142 ± 2	191 ± 4
	1600 K	172 ± 1	145 ± 6	196 ± 2
DFT	0 K	171.2	160.5	153.9

Computed using molecular dynamics simulations at a carbon content of 18.8% in the melt. Shown in units of meV Å⁻². DFT values are obtained from ref. 20.

lower supersaturation the critical nucleus size and the free-energy barrier of nucleation increase. Many of the curves share common characteristics at given values of n due to certain cluster sizes being energetically (geometrically) more favorable than others, the most notable example being the dip at $n = 6$ due to the formation of a C₆ ring.

For comparison of the curves in Fig. 8 with the models developed in Section “Free energy of nucleation”, the interfacial free energies between graphite and the melt must be known. A common approach to estimate solid/liquid interfacial energies is the capillary fluctuation method (CFM)⁵⁴. However, this method requires a large simulation box which in combination with the computationally expensive (paramagnetic) NNP utilized in this work quickly becomes infeasible. An alternative approach is the critical nucleation method, which has been shown to yield similar results⁵⁵ and is directly accessible from the present nucleation simulations using the equations developed in Section “Free energy of nucleation”. For comparison, this work also uses a simpler approach by only considering the enthalpic component of interfacial energies which are directly accessible from MD simulations. The enthalpic component is calculated as the difference between the total energies of simulations of a graphite / melt interface slab system and bulk components divided by the contact area (twice the lateral area). The computed interfacial energies are shown in Table 2. Static DFT interfacial energies from ref. 20 are included as a reference, showing reasonable agreement between the two approaches.

The best agreement between Eq. (13) and the free-energy data (Fig. 8) is obtained by fitting the parameters of the equation to the data. The four optimized parameters and their best-fit values are $g_n = -3.46$ eV atom⁻¹, $x_{eq} = 18.2\%$, $\gamma_{pl} = 138$ meV Å⁻² and $r_0 = 1.45$ Å. The first three of these are in reasonable agreement with their independently computed values of $g_n = -2.69$ eV atom⁻¹, $x_{eq} = 20.0\%$ and $\gamma_{pl} = 142$ meV Å⁻², while r_0 cannot be computed independently. The resulting model curves are plotted as dashed lines in Fig. 8.

The atomic configurations of critical nuclei with $n = 26$ and $n = 50$ along with their local atomic environment from MD simulations are visualized in Fig. 9. The nuclei fluctuate in size through the attachment/

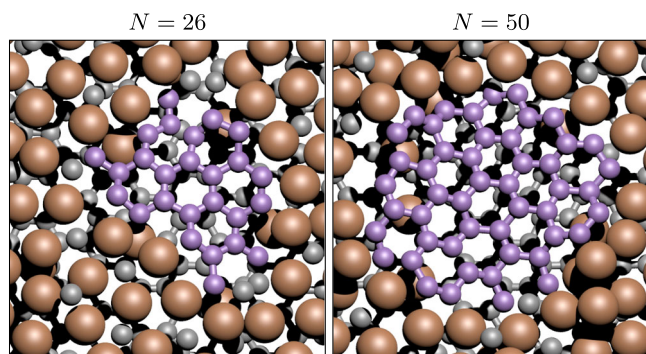


Fig. 9 | Graphite 2-D nucleation at the transition state. Snapshots of critical nuclei with $n = 26$ and $n = 50$ are shown at carbon supersaturations of 8.1% and 4.9% respectively. Only atoms in a thin slab around the 2-D nucleus and the underlying graphene sheet is shown. Carbon atoms constituting the 2-D nucleus are highlighted in magenta.

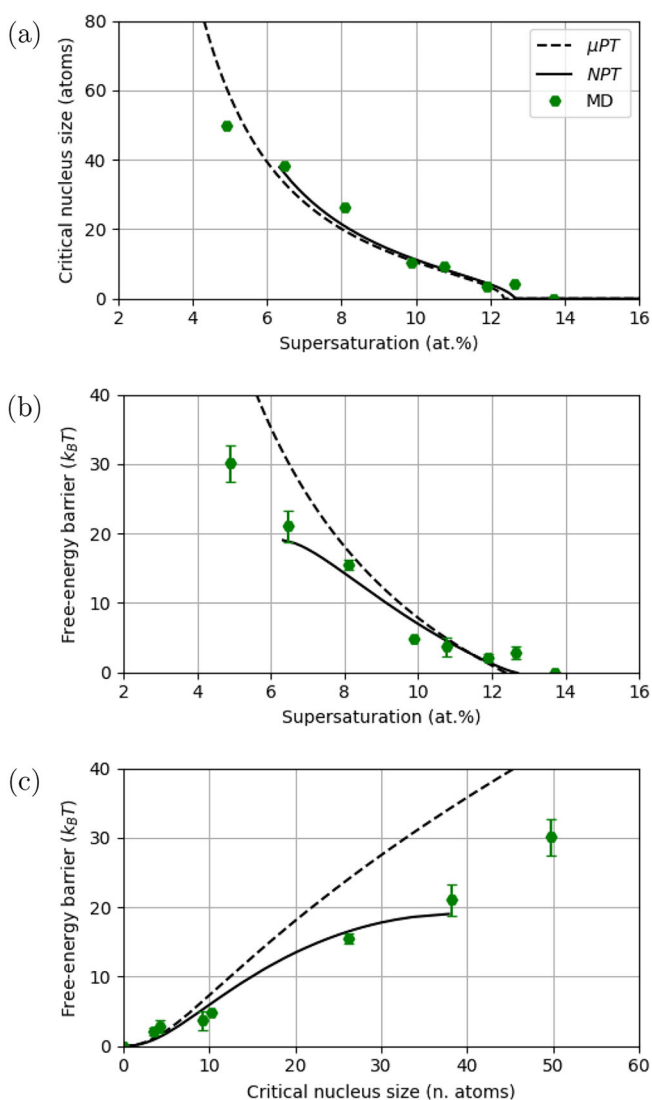


Fig. 10 | Critical nucleus size and free-energy barrier. Scatter points show information about critical nuclei as a function of supersaturation and nucleus size from MD simulations. Black lines are calculated using the 2-D nucleation models developed in the Section “Free energy of nucleation”. The solid line is calculated in the NPT ensemble (relevant to MD) and the dashed line in the μ PT ensemble (appropriate assuming fast diffusion of carbon). Error bars represent the standard deviation of free-energy differences obtained using only the first or the second half of the equilibrated MD trajectories.

detachment of single carbon atoms. Configurations that minimize the number of dangling bonds are preferred, although considerable variation in the shape of the nuclei can be observed. The interaction with the underlying layer of graphite is weak and the nucleus thus moves and rotates relative to the substrate throughout the simulation. Some out-of-plane undulation of the nucleus is also observed, with diffusion of Fe atoms between the substrate and the nucleus. The average distance between the nucleus and the substrate is slightly higher than the equilibrium distance between pristine layers of graphite.

Information about the critical 2-D nuclei is presented in Fig. 10. Scatter points show results from MD simulations, each marker corresponding to the maximum of a free-energy curve shown in Fig. 8. The uncertainties are estimated as the standard deviation of free-energy differences obtained from two 150 ps segments (the first and second halves of the final 300 ps) of each umbrella sampling trajectory used in the WHAM analysis. The dashed and solid lines in Fig. 10 show the model curves in the μ PT and NPT ensembles, i.e., assuming a constant melt composition or number of particles using equations (7) and (13) respectively. Although the NPT model is more representative in the context of MD simulations where the total number of particles is fixed, the μ PT model is more representative during real solidification conditions where the system is free to exchange particles with a large reservoir.

In general, there is good correspondence between the analytical models and the MD simulation results. In Fig. 10a, the critical nucleus size is plotted as a function of supersaturation. As carbon supersaturation decreases, the size of the critical 2-D nucleus increases sharply. At supersaturations below approximately 6 at.%, the NPT curve vanishes due to the small system size (around 1300 atoms in the melt) as growing a sufficiently large 2-D nucleus will excessively deplete the melt from C atoms, never reaching the transition point⁵⁶. This effect prohibits the calculation of nucleation barriers at lower supersaturations with the chosen system size.

In Fig. 10b, the corresponding free-energy barriers are plotted as a function of supersaturation. Similar features are observed as above; however, the μ PT and NPT models diverge at lower supersaturations. In Fig. 10c, the free-energy barrier is plotted against the critical nucleus size demonstrating that although the MD simulation results exhibit some variability, they follow the NPT model more closely than the μ PT model. The limiting values of carbon supersaturation for which the free energy of 2-D nucleation was computed are 4.9 and 13.7%. In the former case, a large critical nucleus comprising 50 C atoms must be reached before free growth can take place, which constitutes a substantial nucleation barrier of $30.1 k_B T$. At a very high supersaturation of 13.7% the barrier for nucleation vanishes, which implies that new layers of graphite can grow freely without nucleation.

Discussion

A paramagnetic NNP was developed for the Fe-C system, and it was verified against various structural and thermodynamic properties of the graphite-austenite-melt system. The NNP has demonstrated success in reproducing several experimentally verifiable properties of the system, and constitutes a valuable model for studying the kinetics of graphite nucleation.

The 2-D nucleation tendency of graphite from the Fe-C melt was computed at various supersaturations of carbon using a combination of MD simulations with free-energy methods. The results were compared to continuum models with parameters obtained from independent simulations and experimental databases, and good agreement was found between the simulations and the continuum models. With the system size chosen for the MD simulations, the lowest supersaturation of carbon for which the nucleation barrier could be computed was 4.9%, corresponding to a carbon content of 23.1%. At this concentration, the critical nucleus consisted of 50 atoms and had a free-energy barrier of $30.1 k_B T$.

Using the available data, the graphite 2-D nucleation rate can be evaluated. Assuming that nucleation may occur in a slab of thickness 3.41 \AA above the substrate, the bulk carbon content translates to a monomer surface density of 7.37 nm^{-2} . The attachment rate of C atoms to the critical nucleus estimated from fluctuations of the nucleus size is 0.14 ps^{-1} , and

based on the second derivative of the free-energy profiles in Fig. 8 the Zeldovich factor is 0.92. Plugging this information into Eq. (10) yields approximately one nucleation event every 10 microseconds on a cubic-micrometer sized substrate. This rate suggests that successive graphite layers can nucleate frequently enough via the 2-D mechanism to sustain growth along the *c*-direction within realistic solidification time scales.

Based on the continuation of the metastable liquidus lines for graphite and austenite (dashed lines in Fig. 7) a 5% supersaturation should only occur at high undercooling. At a moderate undercooling the supersaturation of carbon is around 2% at which the nucleation rates through this mechanism are expected to be too low to account for graphite nucleation or growth. While it is plausible that locally a higher supersaturation can be achieved in a melt due to non-equilibrium conditions induced by, e.g., austenite precipitation, this possibility would require more substantiation.

At low supersaturation, alternative mechanisms for nucleation and growth must be considered. Graphite heterogeneous nucleation may still be supported by an additional chemical affinity between the substrate and graphite, i.e. the middle term in Eq. (7). Another hypothesis is that 2-D nucleation is promoted by solute elements in the melt such as silicon, sulfur, or oxygen. For example, there is evidence suggesting that dissolved surface-active elements such as sulfur can significantly alter the interfacial solid / liquid energies between graphite and the melt^{37,57}. This could consequently reduce the barrier for 2-D nucleation sufficiently to make it a feasible mechanism at lower supersaturation.

A likely alternative is that defects are indeed necessary to initiate the formation of new layers of graphite at a low supersaturation of carbon. In the context of heterogeneous nucleation these defects can, for example, be step-boundaries of the typically observed substrates for graphite such as manganese sulfides in lamellar graphite iron^{38,59}, or (Mg,Ca)-sulfides and (Mg,Al,Si)-nitrides in spheroidal graphite iron^{23,60}. Such defects may provide both a chemical driving force for the initial carbon adsorption and a geometrical benefit of minimizing interfaces with the melt. For graphite growth in the *c*-direction, several defect-controlled mechanisms have already been proposed in the past, as described in the introduction. More research is required to validate these hypotheses, and the methodologies explored in this work, both NNP generation and analytical models, will provide useful tools for understanding the underlying mechanisms of graphite nucleation and growth.

Conclusions

A pragmatic approach starting from first-principles methods for dealing with paramagnetic liquids has been developed and applied to the Fe-C system. A neural-network potential (NNP) was developed for the graphite-austenite-melt system and validated against various structural, elastic, and thermodynamic properties relevant for graphite nucleation. The presented approach for training a paramagnetic NNP relies on performing first spin-polarized DFT simulations for magnetic configurations of liquid snapshots (training set #1) to generate a spin-aware NNP which itself is used to average over a large set of magnetic configurations (training set #2) to train the paramagnetic (spin-averaged) NNP in an iterative fashion. We expect that this approach is readily applicable for extensions to additional elements in the Fe-C system and other paramagnetic liquids.

The equilibrium phase diagram and thermodynamic driving forces were derived from the trained paramagnetic NNP using molecular dynamics simulations combined with free-energy methods. The results were validated against experimentally derived data obtained from the thermochemical software FactSage, and reasonable agreement between the simulation and experimental data was found for the Fe-C system.

Graphite 2-D nucleation was studied as a possible mechanism for graphite growth and as a benchmark case of heterogeneous nucleation. The critical nucleus size and free-energy barrier for nucleation were calculated using MD simulations with umbrella sampling and WHAM, and the results were compared to continuum models based on classical nucleation theory. Good agreement was found between simulation results and the continuum

Table 3 | Summary of the DFT data set used for NNP development

Structure type	No. Configs	Tot. Fe	Tot. C
Fe-C melt	574	14,624	3065
Solid graphite	257	-	8032
Solid austenite	56	1792	-
Graphite (10 $\bar{1}$ 0) / melt	279	3668	6384
Graphite (11 $\bar{2}$ 0) / melt	326	3896	7154
Graphite (0001) / melt	514	5825	10,967
Austenite (111) / melt	26	1222	156

All input configurations were snapshots from MD simulations using lower accuracy force fields, and the forces and energies were evaluated using CP2K.

models, and the relevant parameters were calibrated by several independent methods relying on both experimental and simulation data.

The feasibility of 2-D nucleation to account for graphite heterogeneous nucleation and growth in the solidification of Fe-C alloys was explored. It was found that at 5% or higher supersaturation of carbon new layers of graphene can nucleate on the basal plane of graphite with a sufficient rate to account for these phenomena. At lower supersaturation the nucleation rates decline, and alternative mechanisms must be considered. Heterogeneous nucleation may still occur via 2-D nucleation if the substrate exhibits strong chemical affinity with graphite. Solute elements in the melt may also lower nucleation barriers, facilitating both heterogeneous nucleation and subsequent growth. The alternatives to 2-D nucleation are defect-controlled mechanisms which proceed along more complex, lower-barrier paths that do not rely on the nucleation of new graphene layers. The combination of NNPs and MD simulations is recognized as a valuable tool for further research along these lines.

Methods

Neural-network potential development

Initial atomistic configurations relevant for the Fe-C system were generated using the ASE⁶¹ and pymatgen⁶² tools. The configurations consisted of a combination of bulk solid structures, bulk Fe-C melt and solid/melt interface slab structures. The relevant solid structures included graphite and austenite (γ -Fe). The structures were perturbed by means of short MD simulations to generate inputs for training data. The simulations were initially run using already available classical and universal potentials^{43,47}, and later using the NNP under development as it began to produce stable trajectories. Arbitrary snapshot configurations were selected from the MD trajectories to iteratively generate more training data and improve the quality of the NNP. The perturbed configurations were used as inputs to electronic structure calculations (DFT) to compute the total energies and forces on atoms. A summary of the training data set used for the development of the NNP is shown in Table 3. Structures containing graphite were prioritized over austenite and the emphasis was placed on interface slab structures, as the main objective of this work was to study graphite nucleation at an interface. The AiiDA workflow and provenance management system⁶³ was used to manage calculations and automate workflows throughout this work.

Electronic structure calculations were performed within the framework of density functional theory using the CP2K software package⁶⁴. A hybrid Gaussian and plane waves (GPW) approach was employed to solve the Kohn-Sham equations. Double-zeta valence plus polarization (DZVP) basis set⁶⁵ was used for the Kohn-Sham orbitals and the plane waves for electron density were truncated using a kinetic energy cutoff of 600 Ry. The gradient-corrected PBE exchange-correlation functional⁶⁶ was utilized and the Goedecker-Teter-Hutter (GTH) pseudo-potentials⁶⁷ were employed to approximate core electron interactions. An electronic temperature of 1500 K was applied via Fermi-Dirac smearing to account for thermal occupation of electronic states. Spin-polarized calculations were performed for all configurations, and to address the paramagnetic nature of iron at the

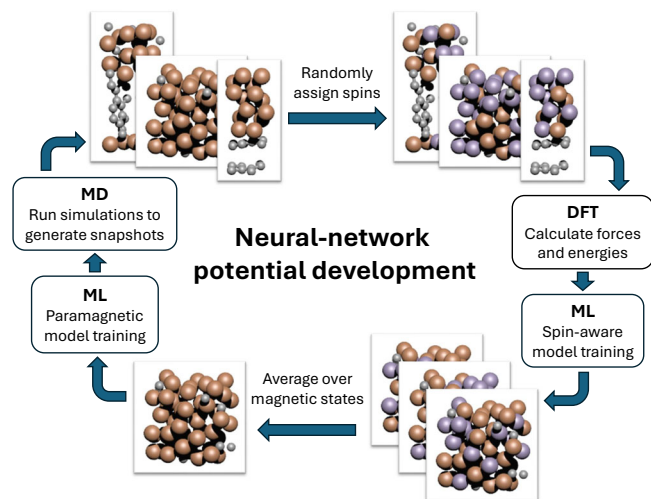


Fig. 11 | Paramagnetic neural-network potential development. The methodology involves using spin-polarized DFT data to train a spin-aware model, and averaging over magnetic states to create a dataset for paramagnetic model training.

temperatures relevant for this work, all iron atoms were randomly assigned an initial excess of spin-up or spin-down electrons of 2.3. While the magnetic moments were allowed to relax during the self-consistent field cycles, they invariably converged to local minima near their initial configurations. The Brillouin zone was sampled using the Monkhorst-Pack scheme ensuring a maximum spacing of 0.25 \AA^{-1} . The D3-correction method by Grimme et al.⁶⁸ was used to address dispersion interactions between graphite layers.

The DFT data set was divided into training and validation sets with an 80–20% split via random sampling. Structures exhibiting maximum forces exceeding 20 eV \AA^{-1} were deemed unphysical and excluded from the dataset. A neural-network potential was developed using the DeePMD-kit software package⁴². The local atomic environment was described using the smooth-edition of the Deep Potential descriptor⁶⁹, with cutoff radius of 6 \AA for neighbor searching and smoothing cutoff of 0.5 \AA . The sizes of the hidden layers in the descriptor network were set to 25, 50 and 100. The fitting network had three hidden layers of 240 neurons each. Training utilized an exponentially decaying learning rate, starting at 0.001 and decaying over 100 steps to a minimum of 3.5×10^{-8} . The loss function prioritized forces with a starting weight of 1000, decaying to 1, while energy contributions started at 0.02 and increased to 1 over time. The training was performed using a batch size of 1200 over 200,000 steps.

A schematic of the training workflow is shown in Fig. 11. To deal with the varying spin moments of iron atoms a spin-aware NNP was first trained by treating spin-up and spin-down iron as distinct types. Spin-inversion symmetry was ensured by duplicating the training data with reversed spin moments. The spin-aware model was then used to sample over different magnetic configurations in the dataset, ensuring that the total spin moment of the system is always close to zero. A spin-averaged data set was created by averaging forces and energies over 1000 magnetic configurations for each atomic configuration, and the final spin-averaged (paramagnetic) NNP was trained on this dataset implicitly accounting for the paramagnetic nature of the system.

The resulting spin-averaged potential has no explicit magnetic degrees of freedom and is therefore not capable of dynamically modeling magnetic excitations, but it is trained on a dataset that statistically represents the paramagnetic state. This approach is conceptually similar to the spin-space averaging (SSA) method⁵⁰, which has been shown to effectively approximate paramagnetic disorder in DFT calculations. While developing accurate paramagnetic models for iron remains challenging even at the DFT level, such ensemble-averaged potentials have been found to be reasonably accurate for modeling high-temperature properties of iron alloys⁷⁰. Since the model only accounts for paramagnetism implicitly, it does not include

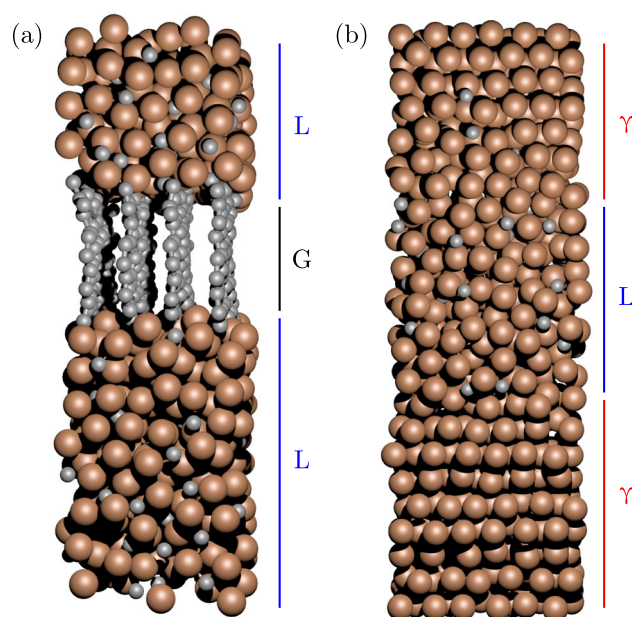


Fig. 12 | Slab models for studying crystallization. The panels show snapshot configurations of graphite (a) and austenite (b) in contact with Fe-C melt, used in co-existence simulations to determine liquidus lines in the phase diagram and driving forces away from equilibrium.

magnetic entropy contributions to the free energy. These contributions can be significant at elevated temperatures, affecting defect formation energies, mixing enthalpies, and diffusion behavior, but capturing them requires more advanced treatments of magnetism and thermodynamics, such as spin dynamics or quantum-statistical models⁷⁰.

Molecular dynamics simulations

Molecular dynamics simulations were performed using the LAMMPS⁷¹ simulation package applying the previously described paramagnetic NNP for the Fe-C system. All simulations were conducted in the NPT ensemble, with temperature and pressure controlled by a Nosé-Hoover thermostat and barostat allowing variations in the simulation box along all three dimensions independently. In calculations of interfacial energies only variation along the z -axis was allowed. The temperature was varied between 1400 and 1600 K and the pressure was set at 1 bar. A time step of 0.5 fs was chosen to ensure stability in the dynamics of the system.

Free-energy calculations were performed using umbrella sampling implemented via the PLUMED⁷² plugin within LAMMPS. Collective variables (CVs) were defined to capture the number of solid carbon (graphite) and iron (γ -Fe) atoms in the system. The former is based on a local average of the self-coordination number of carbon atoms, while the latter was based on the sixth-order Steinhardt parameter⁷³. Details regarding the collective variables used are provided in the Supplementary Information. The umbrella windows were spaced at intervals of one solid carbon atom or five solid iron atoms along the CV. Each simulation was run for a total of 600 ps (graphite) or 300 ps (austenite), with the first half used for equilibration and the second half for production sampling to ensure sufficient coverage of the biased distributions. A harmonic restraint with a force constant of 0.5 eV atom^{-1} was applied for graphite and 0.1 eV atom^{-1} for austenite in each window to maintain the CV near the desired value. Subsequently, free-energy profiles were constructed by integrating biased histograms across windows using the weighted histogram analysis method⁷⁴.

Thermodynamic modeling

For determining the location of phase equilibria, interfaces between pairs of materials were constructed by stacking slabs in the z -direction. Two systems were considered are shown in Fig. 12: equilibrium of the melt with either

solid graphite or austenite, corresponding to the graphite and austenite liquidus lines. The graphite-melt system was constructed with the (3140) plane of graphite facing the melt to minimize the energy barrier for forming partially filled layers of graphite at the interface. The lateral dimension of the system was 13.7 by 17.8 Å consisting of 4 sheets of graphene and 14 slightly tilted rows of carbon atoms, respectively. The austenite-melt system was constructed with the (111) plane of FCC austenite facing the melt and lateral dimensions of 13.4 by 15.5 Å corresponding to 3 and 6 rows of iron atoms in the [112] and [110] directions, respectively. The heights of the slabs varied depending on the specific conditions of the phase diagram sampled, however at 1500 K the equilibrium thicknesses of the solid and liquid slabs were 10.9 and 30.1 Å in the graphite-melt system and 19.5 and 30.8 Å in the austenite-melt system, respectively. The graphite-melt system comprised 560 Fe and 412 C atoms, while the corresponding numbers for the austenite-melt system were 810 Fe and 95 C atoms.

The thermodynamics of the systems were explored as a function of the number of solid atoms. Carbon and iron atoms were transferred between the solid and liquid phases in the graphite-melt and austenite-melt systems, and the free-energy profiles were computed by means of umbrella sampling and WHAM. The locations of phase equilibria were identified as minima of the free-energy profile.

To quantify the driving force ΔG_n that acts to restore the system at a deviation from equilibrium, also known as the difference in chemical potential of the moving species between the two phases (free energy per atom), an expression for the Gibbs free energy with a varying number of solid atoms n_s in the NPT ensemble is required. Assuming that at small deviations the driving force is linearly dependent on the offset from the equilibrium melt composition $\Delta G_n = g_n \Delta x$ the free energy of the system can be expressed as

$$G(n_s) = \int_0^{\Delta n_s} g_n \Delta x(n_s) dn_s \quad (1)$$

where $-\Delta n_s$ is the number of atoms that need to be transferred between two phases to reach equilibrium, Δx is the deviation from equilibrium melt composition and g_n is a proportionality constant. Since the main interest is the precipitation of graphite from a supersaturated melt, the driving force should be expressed in terms of the carbon content in the melt Δx_C which at small Δn_s can be approximated as $\Delta x_C \approx \frac{\Delta n_s}{n_l}$, where n_l is the total number of atoms in the liquid phase. Substituting into (1) one obtains

$$G(n_s) = \int_0^{\Delta n_s} g_n \frac{\Delta n_s}{n_l} dn_s = \frac{g_n \Delta n_s^2}{2n_l} \quad (2)$$

Hence, g_n can be obtained by fitting a parabola to the free-energy profile from the co-existence calculations $G(n_s)$. At higher departures from the equilibrium composition, its more exact form can be used by substituting $\Delta x_C = \Delta n_s / (n_{Fe} - n_C - n_s)$.

To benchmark simulation results against data derived from experiments, the simulations were complemented by thermodynamic calculations using the FactSage database and modeling software⁷⁵. The FSstel database⁵⁷ was utilized to calculate the free energies of graphite and melt as a function of its carbon content. The Gibbs free energy of a system consisting of graphite in molten iron is given by

$$G = n_s G_s + n_l G_l(x_C) \quad (3)$$

where n_s and n_l are the number of particles in the solid and liquid phases, G_s and $G_l(x_C)$ are the Gibbs free energies per mole of the phases and x_C is the carbon content of the melt. To obtain the Gibbs free energy per moles of graphite formed Eq. (3) is differentiated with respect to n_s giving

$$\Delta G_n = \frac{\partial G}{\partial n_s} = G_s + \frac{\partial}{\partial n_s} n_l G_l(x_C) \quad (4)$$

Since the total number of particles must be constant, expressed as $(\delta n_l = -\delta n_s)$, using the product rule yields

$$\Delta G_n = G_s - G_l(x) + n_l \frac{\partial G_l(x_C)}{\partial n_s} \quad (5)$$

To enforce that the number of carbon atoms is also constant, we can write $n_s + n_l x_C = \text{const}$. Differentiating with respect to n_s yields $\partial x_C / \partial n_s = (x_C - 1) / n_l$. Using the chain rule Eq. (5) can then be written as

$$\Delta G_n = G_s - G_l(x) + (x_C - 1) \frac{\partial G_l(x_C)}{\partial x_C} \quad (6)$$

The first and second terms describe the difference between the free energies of graphite and the melt, while the final term accounts for the free energy of changing the composition of the melt. At supersaturations below 15%, ΔG_n is approximately linear as a function of carbon content and g_n can thus be obtained by fitting a linear function to $\Delta G_n(x_C)$.

Free energy of nucleation

The 2-D nucleation model considered in this work consists of the formation of a disc-shaped single atomic layer of graphene on the basal plane of the bulk graphite as shown in Fig. 1. The model has already been presented and applied for graphite growth in the past^{28,29}, and is a special case of the heterogeneous nucleation models proposed in our previous article²⁰.

In the context of MD simulations, this is modeled by initializing a nucleus consisting of a circular sheet of graphene on a double-layer of graphite surrounded by melt in the z-direction. A snapshot of a simulation is presented in Fig. 13 showing only solid C atoms. The size of the nucleus was varied by moving carbon atoms between the nucleus and the melt, and the free energy of nucleation was estimated by means of umbrella sampling and WHAM. Note that since the total number of each species remains fixed within an umbrella sampling series, variations in nucleus size lead to slight changes in the melt composition.

All simulations were run at 1500 K but the melt was initialized with different carbon contents, thus estimating nucleation barriers at various supersaturations of carbon. The simulation box measured 25.4 by 24.4 Å in the lateral direction and varied around 32 Å in the z-direction. The lowest (highest) carbon -containing system consisted of 810 (909) C and 929 (908) Fe atoms. Of these 480 carbon atoms always constituted the double-layer of graphite, while the 2-D nucleus size varied from zero to about 70 carbon atoms.

The simulation results are compared with analytical models based on bulk driving forces and interfacial energies. Following the model introduced in ref. 20, the free-energy change due to the formation of the disc of radius r and thickness t at a constant melt composition (constant μ) is given by

$$\Delta G = r^2 \pi t \Delta G_V + r^2 \pi (\gamma_{bl} + \gamma_{bn} - \gamma_{ln}) + 2r \pi t \gamma_{pl} \quad (7)$$

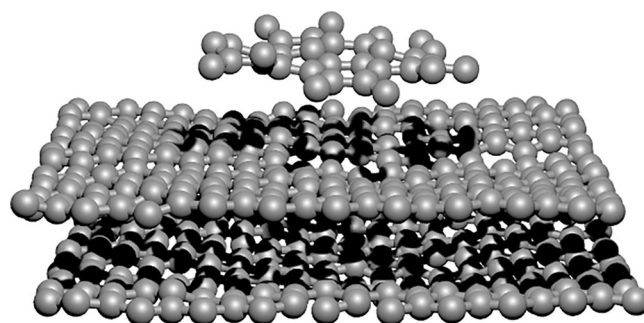


Fig. 13 | Snapshot of a simulation of graphite 2D-nucleation. Iron and carbon atoms in the liquid state are not shown.

where G_V is the volumetric change in free energy due to formation of the solid and γ denotes the interfacial energies between the graphite basal (b) and prismatic (p) planes, the liquid (l) and the nucleant substrate (n). Since the nucleant substrate is here also the basal plane of graphite $\gamma_{bl} = \gamma_{ln}$ and $\gamma_{bn} = 0$, and the middle term vanishes. Solving $\partial G(r)/\partial r = 0$ for r the critical radius $r_c = -\gamma_{pl}/\Delta G_V$ is obtained at the maximum of free energy. The corresponding free-energy barrier for nucleation is

$$\Delta G^* = -\frac{\pi t_0 \gamma_{pl}^2}{\Delta G_V} \quad (8)$$

Following in the lines of classical nucleation theory⁷⁶, if ρ is the surface density of monomers at the liquid-nucleant interface, the density of clusters of critical size is given by

$$\rho_c = \rho e^{-\frac{\Delta G^*}{k_B T}} \quad (9)$$

The nucleation rate J is then computed by multiplying ρ_c by the rate of attachment of the atoms to a critical nucleus $f_{n^*}^+$ and the Zeldovich factor $Z = \sqrt{|\Delta G''(n_c)|/2\pi k_B T^{77}}$ yielding

$$J = \rho f_{n^*}^+ Z e^{-\frac{\Delta G^*}{k_B T}} \quad (10)$$

In finite systems with a fixed number of atoms (constant N) relevant in the context of MD simulations, the composition of the melt can not be assumed as constant. In the more appropriate NPT ensemble, the free energy of nucleation is given by

$$\Delta G = \int_0^{n_i} g_n \Delta x_c dn_s + 2r\pi t \gamma_{pl} \quad (11)$$

where x_C is the carbon content of the melt given by

$$x_C = \frac{n_C - n_s}{n_{Fe} + n_C - n_s} \quad (12)$$

its deviation from equilibrium is given by $\Delta x_C = x_C - x_{eq}$, n_{Fe} and n_C are the numbers of Fe and C atoms in the melt before 2-D nucleation and n_s is the number of C atoms in the 2-D nucleus. Inserting in Eq. (11) and evaluating the integral leads to

$$\Delta G = g_n n_{Fe} \log \frac{n_{Fe} + n_C - n_s}{n_{Fe} + n_C} + g_n n_s (1 - x_{eq}) + 2r\pi t \gamma_{pl} \quad (13)$$

Although Eq. (13) cannot be solved analytically for the critical nucleus size, its numerical solution is trivial.

There is a limitation in the direct applicability of equations (7) and (13) in the limit of forming small nuclei. Consider the formation of a nucleus with radius 0.76 Å which is the covalent radius of carbon. Since this corresponds to a single carbon atom, it is equivalent to carbon in solution with the melt, and its free energy of formation should thus be zero. Nevertheless, using Eq. (7) with $g_n = -0.32 \text{ eV } \text{Å}^{-3}$, $\Delta x_C = 5\%$, $\gamma_{pl} = 140 \text{ meV } \text{Å}^{-2}$ and $t_0 = 3.41 \text{ Å}$ yields a very significant free-energy cost equal to $17k_B T$ at 1500 K. To compensate for this, the free-energy profile can be offset by subtracting the term $-2r_0\pi t \gamma_{pl}$ from equations (7) and (13) where r_0 is a value comparable to the covalent radius of a carbon atom.

Data availability

The datasets generated and analyzed within the current study are available in the Zenodo repository, <https://doi.org/10.5281/zenodo.17431047>.

Received: 23 May 2025; Accepted: 10 November 2025;

Published online: 09 January 2026

References

- Dantzig, J. & Rappaz, M. *Solidification, Second Edition* (Presses Polytechniques et Universitaires Romandes, Lausanne, Switzerland, 2017), 2 edn.
- Elliott, R. *Cast Iron Technology* (Butterworth-Heinemann, Oxford, England, 1988).
- Stefanescu, D. *Science and engineering of casting solidification* (Springer International Publishing, Basel, Switzerland, 2015), 3 edn.
- Stefanescu, D. M., Alonso, G. & Suarez, R. Recent developments in understanding nucleation and crystallization of spheroidal graphite in iron-carbon-silicon alloys. *Met. (Basel)* **10**, 221 (2020).
- Michels, L. et al. Effect of holding time on populations of microparticles in spheroidal graphite irons. *Metall. Mater. Trans. B* **53**, 836–847 (2022).
- Bugten, A. V. et al. Influence of B and Cu on microstructure and eutectoid transformation kinetics in spheroidal graphite cast iron. *Materialia* **43**, 102511 (2025).
- Chen, H., Zhu, W. & Zhang, Z. Contrasting behavior of carbon nucleation in the initial stages of graphene epitaxial growth on stepped metal surfaces. *Phys. Rev. Lett.* **104**, 186101 (2010).
- Fan, Z. & Men, H. An overview on atomistic mechanisms of heterogeneous nucleation. *Met. (Basel)* **12**, 1547 (2022).
- Lekakh, S. N. Understanding heterogeneous nucleation in iron alloys from first principles: A review and discussion. *Int. J. Met.* **19**, 3155–3169 (2025).
- Greer, A. L. Overview: Application of heterogeneous nucleation in grain-refining of metals. *J. Chem. Phys.* **145**, 211704 (2016).
- Xu, Y. et al. Heterogeneous nucleation and grain growth of inoculated aluminium alloys: An integrated study by in-situ X-radiography and numerical modelling. *Acta Mater.* **140**, 224–239 (2017).
- Xu, Y., Casari, D., Mathiesen, R. H. & Li, Y. Revealing the heterogeneous nucleation behavior of equiaxed grains of inoculated Al alloys during directional solidification. *Acta Mater.* **149**, 312–325 (2018).
- Murphy, A. G., Mirihanage, W. U., Browne, D. J. & Mathiesen, R. H. Equiaxed dendritic solidification and grain refiner potency characterised through in situ X-radiography. *Acta Mater.* **95**, 83–89 (2015).
- Tuttle, R. Understanding the mechanism of grain refinement in plain carbon steels. *Int. J. Met.* **7**, 7–16 (2013).
- Fan, Z. & Gao, F. Grain initiation and grain refinement: An overview. *Met. (Basel)* **12**, 1728 (2022).
- Schwarz, M., Karma, A., Eckler, K. & Herlach, D. M. Physical mechanism of grain refinement in solidification of undercooled melts. *Phys. Rev. Lett.* **73**, 1380–1383 (1994).
- Sosso, G. C. et al. Crystal nucleation in liquids: Open questions and future challenges in molecular dynamics simulations. *Chem. Rev.* **116**, 7078–7116 (2016).
- Alonso, G. et al. On the crystallography of the Mg-Si-Al nitride nuclei and of the graphite/nitride interface in spheroidal graphite iron. *Carbon N. Y.* **199**, 170–180 (2022).
- Pires, A. et al. Influence of pre-inoculation treatment on non-metallic micro-inclusion population and microstructure of spheroidal graphite irons. *J. Mater. Sci.* **60**, 4727–4746 (2025).
- Götz, A., Michels, L. & Akola, J. Density functional investigation of the heterogeneous nucleation of graphite on divalent metal oxides and sulfides. *Acta Mater.* **282**, 120427 (2025).
- Turnbull, D. Kinetics of heterogeneous nucleation. *J. Chem. Phys.* **18**, 198–203 (1950).
- Bramfitt, B. L. The effect of carbide and nitride additions on the heterogeneous nucleation behavior of liquid iron. *Metall. Trans.* **1**, 1987–1995 (1970).
- Michels, L. et al. Graphite nucleation on (Al, Si, Mg)-nitrides: Elucidating the chemical interactions and turbostratic structures in spheroidal graphite cast irons. *Carbon N. Y.* **220**, 118848 (2024).

24. Igarashi, Y. & Okada, S. Observation and analysis of the nucleus of spheroidal graphite in magnesium-treated ductile iron. *Int. J. Cast. Met. Res.* **11**, 83–88 (1998).
25. Lacaze, J., Connétable, D. & Castro-Román, M. J. Effects of impurities on graphite shape during solidification of spheroidal graphite cast ions. *Materialia* **8**, 100471 (2019).
26. Stefanescu, D. M., Alonso, G., Larrañaga, P., De la Fuente, E. & Suarez, R. A comparative study of graphite growth in cast iron and in analogous systems. *Int. J. Met.* **12**, 722–752 (2018).
27. Theuwissen, K., Lacaze, J. & Laffont, L. Structure of graphite precipitates in cast iron. *Carbon N. Y.* **96**, 1120–1128 (2016).
28. Amini, S. & Abbaschian, R. Nucleation and growth kinetics of graphene layers from a molten phase. *Carbon N. Y.* **51**, 110–123 (2013).
29. Lacaze, J., Bourdie, J. & Castro-Román, M. J. A 2-D nucleation-growth model of spheroidal graphite. *Acta Mater.* **134**, 230–235 (2017).
30. Double, D. D. & Hellowell, A. Cone-helix growth forms of graphite. *Acta Metall.* **22**, 481–487 (1974).
31. Miao, B., North Wood, D. O., Bian, W., Fang, K. & Fan, M. H. Structure and growth of platelets in graphite spherulites in cast iron. *J. Mater. Sci.* **29**, 255–261 (1994).
32. Kvasnitsa, V. N., Yatsenko, V. & Jaszczak, J. Disclinations in unusual graphite crystals from anorthosites of Ukraine. *Can. Mineralogist* **37**, 951–960 (1999).
33. Sadocha, J. P. & Gruzleski, J. E. Mechanism of graphite spheroid formation in pure Fe-C-Si alloys. In *Proc. 2nd Internat. Symposium on The Metallurgy of Cast Iron*, 1976, 443–459 (1976).
34. Qing, J., Richards, V. L. & Van Aken, D. C. Growth stages and hexagonal-rhombohedral structural arrangements in spheroidal graphite observed in ductile iron. *Carbon N.Y.* **116**, 456–469 (2017).
35. Stefanescu, D. M., Alonso, G., Larrañaga, P., De la Fuente, E. & Suarez, R. Reexamination of crystal growth theory of graphite in iron-carbon alloys. *Acta Mater.* **139**, 109–121 (2017).
36. Shibuta, Y., Oguchi, K., Takaki, T. & Ohno, M. Homogeneous nucleation and microstructure evolution in million-atom molecular dynamics simulation. *Sci. Rep.* **5**, 13534 (2015).
37. Tewary, U. et al. The origin of graphite morphology in cast iron. *Acta Mater.* **226**, 117660 (2022).
38. Blow, K. E., Quigley, D. & Sosso, G. C. The seven deadly sins: When computing crystal nucleation rates, the devil is in the details. *J. Chem. Phys.* **155**, 040901 (2021).
39. Abrikosov, I. A., Ponomareva, A. V., Steneteg, P., Barannikova, S. A. & Alling, B. Recent progress in simulations of the paramagnetic state of magnetic materials. *Curr. Opin. Solid State Mater. Sci.* **20**, 85–106 (2016).
40. Rinaldi, M., Mrovec, M., Bochkarev, A., Lysogorskiy, Y. & Drautz, R. Non-collinear magnetic atomic cluster expansion for iron. *arXiv [cond-mat.mtrl-sci]* 1–12 (2023).
41. Jiang, C., Li, K., Zhang, J., Sun, M. & Bi, Z. Structural characteristics of liquid iron with various carbon contents based on atomic simulation. *J. Mol. Liq.* **342**, 116957 (2021).
42. Zeng, J. et al. DeePMD-kit v2: A software package for deep potential models. *arXiv [physics.chem-ph]* (2023).
43. Batatia, I. et al. A foundation model for atomistic materials chemistry. *arXiv [physics.chem-ph]* (2025).
44. Byggmästar, J. et al. Multiscale machine-learning interatomic potentials for ferromagnetic and liquid iron. *J. Phys. Condens. Matter* **34**, 305402 (2022).
45. Shibazaki, Y. & Kono, Y. Effect of silicon, carbon, and sulfur on structure of liquid iron and implications for structure-property relations in liquid iron-light element alloys. *J. Geophys. Res. Solid Earth* **123**, 4697–4706 (2018).
46. Pan, S., Feng, S., Qiao, J., Dong, B. & Qin, J. The atomic structure of liquid Fe-C alloys. *J. Alloy. Compd.* **648**, 178–183 (2015).
47. Hepburn, D. J. & Ackland, G. J. Metallic-covalent interatomic potential for carbon in iron. *Phys. Rev. B Condens. Matter* **78**, 165115 (2008).
48. Meyer, A., Hennig, L., Kargl, F. & Unruh, T. Iron self diffusion in liquid pure iron and iron-carbon alloys. *J. Phys. Condens. Matter* **31**, 395401 (2019).
49. Lian, C.-S., Wang, J.-T. & Chen, C. Ab initio study of the anharmonic lattice dynamics of iron at the δ -phase transition. *Phys. Rev. B Condens. Matter Mater. Phys.* **92**, 184110 (2015).
50. Körmann, F., Dick, A., Grabowski, B., Hickel, T. & Neugebauer, J. Atomic forces at finite magnetic temperatures: Phonons in paramagnetic iron. *Phys. Rev. B Condens. Matter Mater. Phys.* **85**, 125104 (2012).
51. Liu, Z.-K. Thermodynamics and its prediction and CALPHAD modeling: Review, state of the art, and perspectives. In *Zentropy*, 273–348 (Jenny Stanford Publishing, New York, 2024).
52. Antillon, E. A. & Bernstein, N. Thermodynamical phase-stability of a Cu-Al binary system using machine-learning interatomic potentials. *Phys. Rev. Mater.* **9**, 083801 (2025).
53. van de Walle, A., Sun, R., Hong, Q.-J. & Kadkhodaei, S. Software tools for high-throughput CALPHAD from first-principles data. *CALPHAD* **58**, 70–81 (2017).
54. Hoyt, J. J., Asta, M. & Karma, A. Method for computing the anisotropy of the solid-liquid interfacial free energy. *Phys. Rev. Lett.* **86**, 5530–5533 (2001).
55. Hu, G. et al. Molecular dynamics simulation of solid/liquid interfacial energy of uranium. *J. Nucl. Mater.* **538**, 152183 (2020).
56. Salvalaglio, M., Perego, C., Giberti, F., Mazzotti, M. & Parrinello, M. Molecular-dynamics simulations of urea nucleation from aqueous solution. *Proc. Natl. Acad. Sci. Usa.* **112**, E6–14 (2015).
57. Jung, I.-H., Deckerov, S. A. & Pelton, A. D. A thermodynamic model for deoxidation equilibria in steel. *Metall. Mater. Trans. B* **35**, 493–507 (2004).
58. Riposan, I., Chisamera, M., Stan, S., Hartung, C. & White, D. Three-stage model for nucleation of graphite in grey cast iron. *Mater. Sci. Technol.* **26**, 1439–1447 (2010).
59. Moumeni, E., Stefanescu, D. M., Tiedje, N. S., Larrañaga, P. & Hattel, J. H. Investigation on the effect of sulfur and titanium on the microstructure of lamellar graphite iron. *Metall. Mater. Trans. A* **44**, 5134–5146 (2013).
60. Qing, J., Lekakh, S., Xu, M. & Field, D. Formation of complex nuclei in graphite nodules of cast iron. *Carbon N. Y.* **171**, 276–288 (2021).
61. Hjorth Larsen, A. et al. The atomic simulation environment—a Python library for working with atoms. *J. Phys. Condens. Matter* **29**, 273002 (2017).
62. Ong, S. P. et al. Python materials genomics (pymatgen): A robust, open-source Python library for materials analysis. *Comput. Mater. Sci.* **68**, 314–319 (2013).
63. Huber, S. P. et al. AiiDA 1.0, a scalable computational infrastructure for automated reproducible workflows and data provenance. *Sci. Data* **7**, 300 (2020).
64. Kühne, T. D. et al. CP2K: An electronic structure and molecular dynamics software package - quickstep: Efficient and accurate electronic structure calculations. *J. Chem. Phys.* **152**, 194103 (2020).
65. VandeVondele, J. & Hutter, J. Gaussian basis sets for accurate calculations on molecular systems in gas and condensed phases. *J. Chem. Phys.* **127**, 114105 (2007).
66. Perdew, J. P., Burke, K. & Ernzerhof, M. Generalized gradient approximation made simple. *Phys. Rev. Lett.* **77**, 3865–3868 (1996).
67. Goedecker, S., Teter, M. & Hutter, J. Separable dual-space gaussian pseudopotentials. *Phys. Rev. B Condens. Matter* **54**, 1703–1710 (1996).
68. Grimme, S., Antony, J., Ehrlich, S. & Krieg, H. A consistent and accurate ab initio parametrization of density functional dispersion

- correction (DFT-D) for the 94 elements H-pu. *J. Chem. Phys.* **132**, 154104 (2010).
69. Zhang, L. et al. End-to-end symmetry preserving inter-atomic potential energy model for finite and extended systems. *arXiv [physics.comp-ph]* (2018).
70. Hickel, T. et al. Magnetism in iron alloys: methodological advances for thermodynamics, defects, and kinetics. *Int. J. Mat. Res. (Z. Metallkd.)* **116**, 474–525 (2025).
71. Thompson, A. P. et al. LAMMPS - a flexible simulation tool for particle-based materials modeling at the atomic, meso, and continuum scales. *Comput. Phys. Commun.* **271**, 108171 (2022).
72. Tribello, G. A., Bonomi, M., Branduardi, D., Camilloni, C. & Bussi, G. PLUMED 2: New feathers for an old bird. *Comput. Phys. Commun.* **185**, 604–613 (2014).
73. Steinhardt, P. J., Nelson, D. R. & Ronchetti, M. Bond-orientational order in liquids and glasses. *Phys. Rev. B* **28**, 784 (1983).
74. Pallath, A. WHAM: Python package to construct free energy profiles from biased molecular simulation data using both log-likelihood maximization and self-consistent iteration approaches.
75. Bale, C. W. et al. Reprint of: FactSage thermochemical software and databases, 2010-2016. *CALPHAD* **55**, 1–19 (2016).
76. Song, H., Sun, Y., Zhang, F., Wang, C. Z. & Mendeleev, M. I. Nucleation of stoichiometric compounds from liquid: the role of the kinetic factor. *Phys. Rev. Mater.* **2**, 8 (2018).
77. Auer, S. & Frenkel, D. Prediction of absolute crystal-nucleation rate in hard-sphere colloids. *Nature* **409**, 1020–1023 (2001).
78. Khaliullin, R. Z., Eshet, H., Kühne, T. D., Behler, J. & Parrinello, M. Graphite-diamond phase coexistence study employing a neural-network mapping of the ab initio potential energy surface. *Phys. Rev. B Condens. Matter Mater. Phys.* **81** (2010).
79. von Lilienfeld, O. A., Tavernelli, I., Rothlisberger, U. & Sebastiani, D. Optimization of effective atom centered potentials for London dispersion forces in density functional theory. *Phys. Rev. Lett.* **93**, 153004 (2004).
80. Müller, M., Erhart, P. & Albe, K. Analytic bond-order potential for bcc and fcc iron-comparison with established embedded-atom method potentials. *J. Phys. Condens. Matter* **19**, 326220 (2007).
81. Schäfer, H. J. donohue: The structures of the elements, John Wiley & sons/new york, sydney, toronto 1974, 436 S., preis: £ 12.-. *Ber. Bunsenges. Phys. Chem.* **79**, 110–110 (1975).
82. Seldin, E. J. & Nezbeda, C. W. Elastic constants and electron-microscope observations of neutron-irradiated compression-annealed pyrolytic and single-crystal graphite. *J. Appl. Phys.* **41**, 3389–3400 (1970).
83. Acet, M., Zähres, H., Wassermann, E. F. & Pepperhoff, W. High-temperature moment-volume instability and anti-invar of gamma-Fe. *Phys. Rev. B Condens. Matter* **49**, 6012–6017 (1994).
84. Zarestky, J. & Stassis, C. Lattice dynamics of gamma-Fe. *Phys. Rev. B Condens. Matter* **35**, 4500–4502 (1987).
85. Marqués, M., González, L. E. & González, D. J. Ab initio study of the structure and dynamics of bulk liquid Fe. *Phys. Rev. B Condens. Matter Mater. Phys.* **92** (2015).
86. Schenk, T., Holland-Moritz, D., Simonet, V., Bellissent, R. & Herlach, D. M. Icosahedral short-range order in deeply undercooled metallic melts. *Phys. Rev. Lett.* **89**, 075507 (2002).
87. Inui, M., Maruyama, K., Kajihara, Y. & Nakada, M. Icosahedral ordering in liquid iron studied via x-ray scattering and monte carlo simulations. *Phys. Rev. B* **80**, 180–201 (2009).
88. Waseda, Y. The structure of non-crystalline materials. *Liquids and Amorphous Solids* (1980).
89. Neuhaus, J., JürgenandLeitner, MichaelandNicolaus, KarlandPetry, WinfriedandHennion, BernardandHiess, Arno Role of vibrational entropy in the stabilization of the high-temperature phases of iron. *Phys. Rev. B* **89**, 184302 (2014).

Acknowledgements

This research was funded by the Norwegian Research Council project 341069 with the partners Elkem Silicon Products, NTNU, SINTEF, and Mandal Castings AS. The authors acknowledge Sylvain Gouttebroze at SINTEF, Ragnvald Mathiesen at NTNU, and Gro Eide, Emmanuelle Ott, Cathrine Hartung, Kenneth Friestad, and Bruno Eggert at Elkem Silicon Products for their support. The calculations were performed on resources provided by Sigma2 - the National Infrastructure for High Performance Computing and Data Storage in Norway (project NN10056K), and CSC - IT center for Science, Finland (LUMI supercomputer, project 462000754).

Author contributions

A.G. developed the neural-network potential, ran all simulations and wrote the main manuscript text. D.M. assisted with software setup, performed validation of the potential and wrote Section "Neural-network potential validation". J.A. supervised the project, contributed to the selection of computational tools, and provided regular feedback during the research process. L.M. co-supervised the project and provided guidance on the scientific focus and relevance of the modeled system. All authors reviewed the manuscript.

Funding

Open access funding provided by NTNU Norwegian University of Science and Technology (incl St. Olavs Hospital - Trondheim University Hospital).

Competing interests

The authors declare no competing interests.

Additional information

Supplementary information The online version contains supplementary material available at <https://doi.org/10.1038/s43246-025-01018-4>.

Correspondence and requests for materials should be addressed to Adam Götz.

Peer review information *Communications Materials* thanks Ujjal Tewary and the other, anonymous, reviewer(s) for their contribution to the peer review of this work.

Reprints and permissions information is available at <http://www.nature.com/reprints>

Publisher's note Springer Nature remains neutral with regard to jurisdictional claims in published maps and institutional affiliations.

Open Access This article is licensed under a Creative Commons Attribution 4.0 International License, which permits use, sharing, adaptation, distribution and reproduction in any medium or format, as long as you give appropriate credit to the original author(s) and the source, provide a link to the Creative Commons licence, and indicate if changes were made. The images or other third party material in this article are included in the article's Creative Commons licence, unless indicated otherwise in a credit line to the material. If material is not included in the article's Creative Commons licence and your intended use is not permitted by statutory regulation or exceeds the permitted use, you will need to obtain permission directly from the copyright holder. To view a copy of this licence, visit <http://creativecommons.org/licenses/by/4.0/>.

© The Author(s) 2025